

Efficient HDR Reconstruction from Real-World Raw Images

Qirui Yang¹, Yihao Liu^{*2}, and Jingyu Yang^{†1}

¹Electrical and Information Engineering, Tianjin University

²University of Chinese Academy of Sciences

Abstract

High dynamic range (HDR) imaging is still a significant yet challenging problem due to the limited dynamic range of generic image sensors. Most existing learning-based HDR reconstruction methods take a set of bracketed-exposure sRGB images to extend the dynamic range, and thus are computational- and memory-inefficient by requiring the Image Signal Processor (ISP) to produce multiple sRGB images from the raw ones. In this paper, we propose to broaden the dynamic range from the raw inputs and perform only one ISP processing for the reconstructed HDR raw image. Our key insights are threefold: (1) we design a new computational raw HDR data formation pipeline and construct the first real-world raw HDR dataset, RealRaw-HDR; (2) we develop a lightweight-efficient HDR model, RepUNet, using the structural re-parameterization technique; (3) we propose a plug-and-play motion alignment loss to mitigate motion misalignment between short- and long-exposure images. Extensive experiments demonstrate that our approach achieves state-of-the-art performance in both visual quality and quantitative metrics.

1. Introduction

Most commodity cameras have low dynamic ranges (LDR) and cannot capture the full range of brightness and color information in real-world scenes. In contrast, high dynamic range (HDR) imaging aims to capture a much wider range of luminance values, compensating for the color distortions and the loss of subtle details in LDR images. Although we can directly obtain HDR images with dedicated hardware, they are usually expensive, limiting the practicality for most users. Therefore, fusion-based HDR imaging methods for LDR cameras have received increasing attention.

Most widely-practiced HDR reconstruction methods [16] exploit a sequence of sRGB images with different exposure levels to generate an HDR image. However, in practice, capturing multiple LDR images with varying exposures can present challenges, especially when there is a global movement of the camera or moving objects in the viewfinder frame [16]. To address this issue, Sony has developed a Digital Overlap (DOL) [40] HDR sensor and a Binned Multiplexed Exposure (BME) HDR sensor [23]. These sensors can shorten the time interval between differently exposed images, enabling the “quasi-synchronous” output of multiple frames of raw images with different exposure times. However, the quasi-sync still has the relative motion of the pre-and post-frames, which causes artifacts in the generated HDR image.

Although sRGB-based HDR reconstruction methods [37, 21, 38] have made significant progress in recent years, they tend to overlook three critical aspects. First, as shown in Fig. 1, when obtaining raw LDR images with different exposures, the ISP pipeline [2] must be performed separately on each exposure. This not only incurs additional memory and computational overhead but also leads to lower frame rates for HDR image output. Second, many existing methods [16, 19] replace the complex camera response curve with a simple inverse gamma operation to obtain a set of linear sRGB images. However, this approach may result in different exposure images without luminance alignment in non-saturated regions, making the training more challenging. Third, raw images contain more delicate details of the original sensor signal that can be lost during the processing of sRGB images. The limitations of current HDR reconstruction methods highlight the need for further research and development in HDR imaging.

Based on the above observations, we propose a new scheme for HDR image reconstruction in the raw image domain, which comprises three essential components: a raw HDR image acquisition pipeline, a corresponding training and testing dataset (RealRaw-HDR), and an efficient raw HDR reconstruction network. By analyzing the HDR image

^{*}The first two authors are co-first authors

[†]Corresponding author, E-mail: yjy@tju.edu.cn

sensor system, we discover that changing the Gain of the image sensor can have a similar effect as modifying the exposure time under some conditions. Leveraging this insight, we develop a software imaging system that captures raw images with different exposures, based on a digital camera photoelectric signal conversion model. This manually operable system satisfies real-world scenes’ dynamic range requirements, making it a practical tool for generating high-quality HDR images. The resulting RealRaw-HDR dataset includes a substantial number of LDR-HDR pairs for training and evaluation. By incorporating the unique characteristics of raw images into our approach, we can achieve superior HDR reconstruction results with increased efficiency and accuracy.

To further promote the HDR imaging system, we develop a lightweight and efficient model for raw HDR reconstruction named RepUNet. RepUNet adopts reparameterization techniques and does not contain computationally expensive alignment modules, such as optical flow [16], deformation convolution [5], or attention [19, 39], which are commonly used in existing deep learning-based HDR reconstruction methods [16, 19, 35, 25]. To compensate for the absence of alignment modules, we introduce a plug-and-play motion alignment loss (MA), which encourages the network to focus on local motion patterns and alleviate misalignment between short- and long-exposure images. Consequently, our approach significantly reduces hardware costs and improves the real-time performance of HDR imaging systems.

Our contributions are summarized as follows: (1) We propose a novel computational photography-based pipeline for raw HDR image formation and construct the first real-world raw HDR dataset – RealRaw-HDR. (2) We use structural re-parameterization techniques to develop a lightweight model, RepUNet, which significantly reduces the computational cost of hardware devices. (3) We introduce a plug-and-play motion alignment loss to mitigate misalignment between short- and long-exposure images. Our contributions represent a significant step forward in raw HDR image reconstruction research, providing an effective and efficient solution for producing high-quality HDR images. Extensive experiments demonstrate that our approach achieves state-of-the-art performance in terms of both visual quality and quantitative metrics.

2. Related Work

2.1. HDR Imaging

Extending the camera’s dynamic range has been an important research area in the past decades. One class of technology [32, 30] is to achieve HDR image capture in a single shot by improving the design of digital camera hardware. For example, the Dual Conversion Gain (DCG) sensor [15]

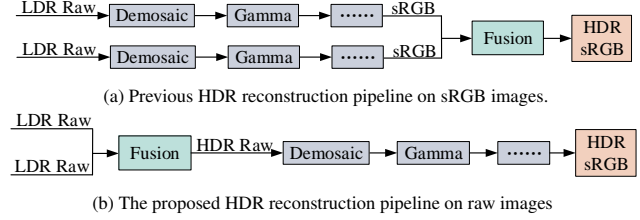


Figure 1. Comparison of HDR reconstruction pipeline on sRGB and raw images.

enhances the camera’s dynamic range through DCG circuitry to ensure that the image sensor can capture images in extreme low-light conditions without sacrificing performance in high-light conditions. Sun et al. [32] propose a method to achieve single-exposure HDR imaging through the end-to-end design of optical coding. Unfortunately, each method requires adapting to particular optical systems or image sensors. These HDR methods with hardware modification are usually expensive and unavailable to average users.

Another category of approaches [24, 19, 35] is the time-domain multi-frame HDR technique, which merges a set of LDR images of the same scene taken at different exposures to obtain an HDR image. This requires the camera to capture images from underexposed to overexposed configurations, which would cause blurring artifacts for moving objects. Therefore, to shorten the time interval between captured images, Sony proposed a Digital Overlap (DOL) HDR sensor [6]. Taking a two-exposure DOL sensor as an example, the sensor outputs long-exposure frames and short-exposure frames in a line interleaving pattern, which significantly shortens the time interval between long-exposure images and short-exposure images, thus reducing the relative motion between the two images. Most approaches nowadays use DOL sensors to capture a set of bracketed LDR images and then merge the multi-exposure LDR images to reconstruct an HDR image.

A recent trend in HDR imaging is to use deep neural networks [18, 25] to learn to produce a high-quality HDR image from a set of exposure-bracketed LDR images. Kalantari et al. [16] propose a CNN-based HDR approach using optical flow to align LDR images before the network inference. Wu et al. [35] treat HDR imaging as an image translation problem without explicit motion alignment. Yan et al. [36] introduce spatial attention to achieve LDR image alignment. Liu et al. [19] propose an attention-guided deformable convolutional network for multi-frame HDR imaging. Prabhakar et al. [28] propose an efficient method to generate HDR images using a bilateral guided up-sampler and further explore zero-learning for HDR reconstruction. Niu et al. [26] propose a multi-frame HDR imaging method under the framework of generative adver-

serial learning. Liu et al. [20] suggest a Transformer-based [27] HDR imaging method. These approaches [36, 19, 20] based on deep learning steadily boost state-of-the-art performance. However, all of these approaches require the ISP pipeline to process multiple-exposed raw images and store them in the random access memory (RAM), which is computationally and memory demanding.

2.2. Low-level Raw Image Processing

Learning-based processing of low-level raw images has received increasing attention. Zhang et al. [42] construct a real-world super-resolution dataset by designing an optical zoom system and propose a baseline network with a bilateral contextual loss. Qian et al. [29] solve the joint demosaicing, denoising, and super-resolution task with the raw input. Wang et al. [33] propose a lightweight and efficient network for raw image denoising. Sharif et al. [1] propose a new learning-based approach to tackle the challenge of joint demosaicing and denoising on image sensors. Wei et al. [34] investigate the low-light image denoising considering sensor's photoelectric properties. Yue et al. [41] achieve state-of-the-art raw image denoising by constructing a dynamic video dataset with noise-clean pairs. Learning-based raw image processing has demonstrated its great potential for high-performance reconstruction from raw sensor data. However, it is difficult and expensive to acquire paired data in the raw domain. Our work proposes a new pipeline to acquire raw HDR-paired data.

3. New Pipeline for Raw HDR Data Formation

We first analyze the sensor response of the imaging system and propose a new formation pipeline for raw HDR-paired data based on the camera response model.

3.1. Analysis of CMOS Imaging System

The essence of a CMOS image sensor is photo-electric signal conversion. For a single pixel, the number of electrons Q released after the light-electric signal conversion can be ideally expressed as [11]:

$$Q = T \int_{\lambda} \int_x \int_y E(x, y, \lambda) S(x, y) q(\lambda) dx dy d\lambda, \quad (1)$$

where (x, y) are spatial coordinates of the sensor plane, T is the integration time (exposure time), $E(x, y, \lambda)$ is the incident spectral irradiance, $S(x, y)$ is the spatial response of the collection site, and $q(\lambda)$ is defined as the ratio (electrons/Joule) of electrons collected per incident light energy for the sensor as a function of wavelength λ .

Since (x, y) in Eq. 1 are restricted to a single photosensory cell, it is assumed that each parameter does not change with position, thus, the coordinates (x, y) can be omitted

[13]:

$$Q = T \bar{S} A \int_{\lambda} E(\lambda) q(\lambda) d\lambda, \quad (2)$$

where \bar{S} denotes the expected value of $S(x, y)$ within a single photosensory cell, and A denotes the effective photoreceptor area of the cell.

Afterward, the electrical signal is amplified by the camera's amplifier circuit, and the raw camera response value is obtained through analog-to-digital conversion [45]:

$$D = \frac{K_a Q + V_{\text{offset}}}{\eta} \times K_d, \quad (3)$$

where K_a denotes the Analog Gain, K_d denotes the Digital Gain, V_{offset} represents the bias voltage. η denotes the quantization step related to the bit depth.

Combining Eq. 2 and Eq. 3, the ideal conversion model of the optical signal to digital signal is modeled as:

$$D = \frac{K_a T \bar{S} A \int_{\lambda} E(\lambda) q(\lambda) d\lambda + V_{\text{offset}}}{\eta} \times K_d, \quad (4)$$

where D is the pixel value in the raw image, V_{offset}/η represents the artificially added bias voltage to avoid output signals lower than 0. The raw response value of the bias voltage (i.e., black level) can be read out directly. When the dark current is 0, or we subtract the raw response value of the bias voltage, we observe from Eq. 4 that, under noise-free conditions, changing the gain factors (K_a, K_d) can achieve the same raw camera response value as changing the exposure time (T). Based on this rationale, we propose a novel and efficient pipeline for generating LDR-HDR data pairs.

3.2. Formation of Raw LDR-HDR Image Pair

Compared to sRGB images, HDR reconstruction from raw images has the advantages of more original information, simpler ISP processing, and less computation, making it a promising paradigm to deploy in edge devices. To this end, we construct the first raw HDR dataset with LDR-HDR data pairs, named RealRaw-HDR.

Data Acquisition. Based on the analysis in Sec. 3.1, we find that changing the Gain can achieve a similar effect as changing the exposure time when the noise level is small. To minimize the influence of noise, we use a high-end FUJI-FILM GFX50S II camera to capture high-quality raw images, and the camera's ISO values are less than or equal to 400. The camera has a 51 megapixel medium format image sensor with a pixel size of $5.3\mu\text{m}$ (The iPhone 14 Pro Max primary camera single pixel size is only $1.22\mu\text{m}$). To avoid an unexpected camera shake, the camera is fixed on a tripod, and the shutter is controlled by a remote smartphone. We trigger the shutter twice in a very short interval to obtain two raw images. Afterward, the raw images are

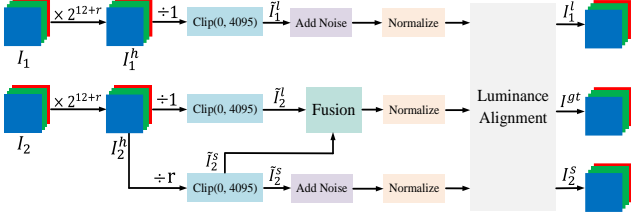


Figure 2. The raw HDR data formation pipeline.

black level corrected, normalized, and then processed with BM3D [22] to reduce noise, which obtains nearly noise-free raw images. Note that there is a small relative motion between these two raw images, which is common in multi-frame HDR reconstruction.

Data Processing. The proposed data formation pipeline is shown in Fig. 2. First, we pack the two Bayer raw images and randomly select an exposure time ratio r from $[4, 8, 16]$. We multiply the two raw LDR images I_1 and I_2 by the maximum pixel value (2^{12+r}), obtaining I_1^h and I_2^h , respectively. This operation is equivalent to adjusting the gains (K_a, K_d), which can achieve a similar effect as changing the exposure time. Second, we divide I_1^h by 1 and I_2^h by r , after which the pixel values are clipped to $[0, 4095]$, resulting in a 12-bit long-exposure image I_1^l and a short-exposure image I_2^s . Moreover, to generate the ground-truth raw HDR image, we divide I_2^h by 1 and clip it to $[0, 4095]$ to form another long-exposure image I_1^l . Then, by combining I_1^l and I_2^s , we generate the corresponding clean raw HDR image using triangle functions as blending weights [16]. In real scenes, noises are inevitable. To simulate such cases, we additionally add noise to I_1^l and I_2^s . Finally, after normalization and luminance alignment [16], we obtain the noisy raw LDR images I_1^l and I_2^s , and the corresponding clean raw HDR image I^{gt} .

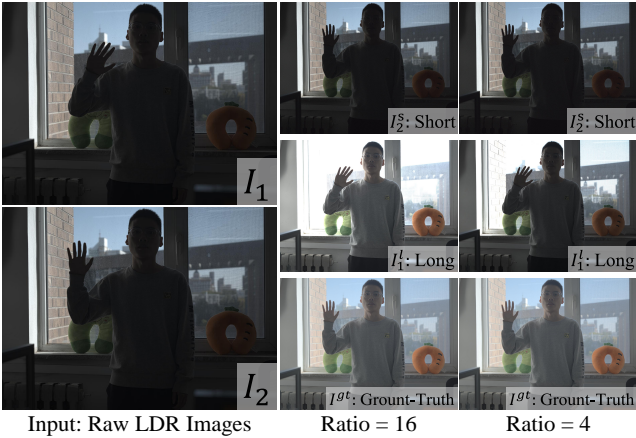


Figure 3. Real samples collected by the proposed raw HDR data formation pipeline.

The proposed pipeline for generating HDR data is ef-

ficient and user-friendly, allowing easy generation of numerous high-quality data pairs. In contrast, the traditional method of adjusting exposure time is limited in its ability to produce arbitrary exposure ratios and is also labor-intensive. Through this pipeline, we collect 240 pairs of 8192×6192 high-resolution raw LDR-HDR image pairs. Fig. 3 shows an example of two generated LDR-HDR pairs with different exposure ratios. It is worth noting that we can also synthesize the sRGB-based HDR training dataset if the ISP pipeline is connected at the end of our pipeline.¹

4. The Proposed RepUNet Network

HDR reconstruction plays a vital role in various applications, such as mobile photography, high-definition displays, and virtual reality, where lightweight and efficient algorithms are highly demanded due to resource limitations. Previous learning-based HDR methods [20, 19, 35] often rely on large and complex models, making them impractical for real-world scenarios. To address this challenge, we propose a UNet-like lightweight base model and employ re-parameterization techniques to improve its representation capability while balancing storage and computation cost and reconstruction accuracy. We first present the base model, and then develop our RepUNet by re-parameterization, followed by the design of loss function.

4.1. Base Model

The overall architecture of the base model is shown in Fig. 4(a). For lightweight design, we do not use the computationally demanding explicit alignment in our HDR network. To compensate for the absence of alignment modules, we introduce a self-guided motion alignment loss (in Sec. 4.3) that enables training with unaligned pairs.

For low computational complexity, we first employ the pixel unshuffle operation [10] to transfer the input raw images I_1^l and I_2^s from $C \times H \times W$ to $4C \times \frac{1}{2}H \times \frac{1}{2}W$. Short-exposure images have less motion blur distortion; long-exposure images generally contain more information with a higher signal-to-noise ratio but may suffer from significant motion blur and overexposure. To better leverage the complementary information from the two images, we introduce two sub-encoders: Encoder-S and Encoder-L. Encoder-S extracts features from the short-exposure image, serving as reference features, while Encoder-L extracts features from the long-exposure image, serving as supplementary features. We fuse the multi-scale features using addition or concatenation operations at each feature level to facilitate complementary features to learn motion information from the reference features. Each Encoder-S consists of a pixel unshuffle $\downarrow 2$ downsampling operation, a 3×3

¹If not specified, all raw images in this paper have been processed by a fixed ISP to obtain sRGB versions for visualization purposes.

convolution layer, and a ReLU activation ([Down-Conv-ReLU]). At the same time, the Encoder-L has the structure of [Down-Conv-ReLU-Conv-ReLU]. The pixel unshuffle operation can avoid information loss introduced by conventional downsampling/pooling operations. Finally, the fused features are fed into the decoder to generate the final HDR output.

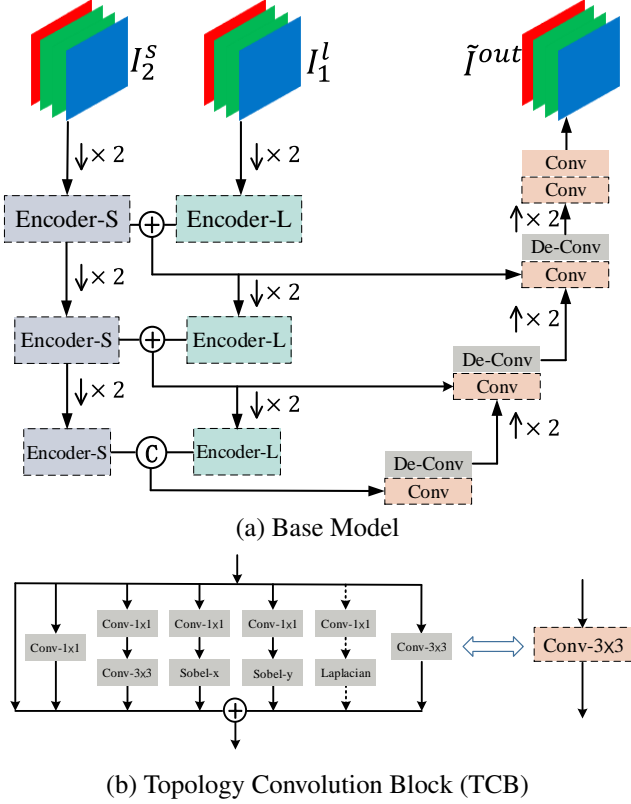


Figure 4. Illustration of (a) Base Model and (b) Topology Convolution Block (TCB). In the training phase, the normal convolution in the dashed box is replaced with a TCB, and the TCB is merged into a normal 3×3 convolution layer in the inference phase.

4.2. RepUNet Network

The representation capability of the plain base model for HDR imaging is limited, leading to unsatisfactory performance. To overcome this limitation, we propose a flexible re-parameterizable module, the Topological Convolution Block (TCB), inspired by previous works [9, 4, 7, 44]. The TCB replaces normal convolution in the base model during training and employs six types of operators to enrich the model’s feature representation.

The TCB includes the following basic units: (1) a normal 3×3 convolution to ensure base performance, (2) extending and squeezing convolution to improve feature expressiveness, (3) Sobel and Laplacian operators to extract first-order and second-order spatial derivatives for edge in-

formation extraction, (4) jump connection to avoid gradient vanishing or exploding, and (5) 1×1 convolution promotes information interaction between channels. Importantly, we use TCB with Laplacian operator only in the decoder since it is only applicable to noise-free images.

After training, we merge TCB re-parameterization into a single 3×3 convolution for efficient deployment and inference. Following previous works [44, 8, 9, 7], we merge the 1×1 extending and 3×3 squeezing convolution into a normal 3×3 convolution, and the Sobel and Laplacian operators into a special 3×3 convolution with a fixed convolution kernel. The 1×1 convolution is achieved by padding the convolution kernel with zeros, and the TCB can thus be transformed into a single 3×3 convolution for efficient implementation at the inference stage. By employing TCB, we achieve superior HDR results with improved efficiency.

4.3. Loss Functions

Motion Alignment Loss. As described in Sec. 4.1, to ensure fast inference and easy deployment on hardware, we do not include an explicit alignment module in the base model. To compensate for this limitation, we propose a plug-and-play motion alignment loss that addresses image alignment problem. We randomly select small squares of size $[40, 60]$ from non-reference frame patches (long exposure) and move them 30 pixels at any angle with varying degrees of motion blur to simulate real object motion. We use a mask M to record the square’s position before and after the movement. We employ the MSSSIM loss [14] to optimize the network and encourage it to pay more attention to local motion regions.

$$L_{MA} = 1 - MSSSIM(\tilde{I}^{out} \odot M, I^{gt} \odot M), \quad (5)$$

where \odot denotes the point-wise multiplication.

Reconstruction Loss. The L2 loss and MSSSIM loss are adopted to ensure the fidelity of predicted raw HDR images and their ground truth.

$$L_{pix} = \|\tilde{I}^{out} - I^{gt}\|_2, \quad (6)$$

$$L_{ssim} = 1 - MSSSIM(\tilde{I}^{out}, I^{gt}). \quad (7)$$

Bayer Loss. we propose a color correction loss, named Bayer loss, to minimize color cast and artifacts. We average the two G channels of the output (RGGB pattern) and ground truth (RGGB pattern) respectively, and then concatenate the averaged G channel with the R and B channels to perform a naive transformation to the RGB color space, producing two RGB images: \tilde{I}_{rgb}^{out} and I_{rgb}^{gt} . Then, we impose the color loss between the processed output and ground truth by the cosine embedding loss.

$$L_b = \text{Cosine}(\tilde{I}_{rgb}^{out}, I_{rgb}^{gt}), \quad (8)$$

Table 1. Performance comparison of different HDR models on our test dataset. The FLOPs and Run Times are measured on the raw image of 4096×2952 resolution. The best and second-best performances are in bold and in underline, respectively.

Methods	FLOPs	Params	Run Times	All-Exposure		Ratio=4		Ratio=8		Ratio=16	
				PSNR \uparrow	$\Delta E \downarrow$	PSNR \uparrow	$\Delta E \downarrow$	PSNR \uparrow	$\Delta E \downarrow$	PSNR \uparrow	$\Delta E \downarrow$
DeepHDR[35]	2409.32G	15.26M	4.3 ms	43.3680	1.3767	43.5551	1.3844	43.7312	1.3679	42.8178	1.3779
NHDRNet[39]	826.17G	40.26M	7.9 ms	33.0206	2.7308	33.0127	2.7277	33.0392	2.7203	33.0101	2.7443
UNet-SID[3]	<u>640.89G</u>	7.76M	<u>3.1 ms</u>	44.3892	1.3434	44.3314	1.3535	44.4551	1.3312	44.3811	1.3456
SGN[10]	712.66G	4.78M	3.3 ms	44.6094	1.3235	44.5074	1.3398	44.7078	1.3067	44.6131	1.3240
AHDRNet[36]	2848.29G	<u>0.93M</u>	23.6 ms	44.7985	<u>1.2939</u>	44.8548	1.2957	44.8343	1.2892	44.7064	1.2968
Ours	127.55G	0.82M	2.9 ms	44.8081	1.2886	<u>44.7575</u>	<u>1.3000</u>	44.8482	1.2812	44.8187	1.2842



Figure 5. Visual comparison of state-of-the-art HDR reconstruction methods on RealHDR-Raw dataset.

where Cosine denotes cosine embedding loss [31]. The overall loss function is

$$L = \alpha \cdot L_{MA} + \beta \cdot L_b + \gamma \cdot L_{pix} + \eta \cdot L_{ssim}. \quad (9)$$

α , β , γ , and η are the corresponding weight coefficients.

5. Experiments

5.1. Datasets and Metrics

Datasets. We utilize the proposed RealRaw-HDR dataset for training. For testing, we select 10 sets of images for cropping and construct 10 sets of three different exposure ratio test samples (i.e., 4, 8, and 16). The training and testing data do not overlap. Furthermore, we also adopt Chen’s test dataset [5] for cross-validation, where the raw images are denoised by BM3D [22] fine-tuning.

Table 2. Performance comparison of different HDR models on Chen’s dataset [5].

Methods	All-Exposure		Ratio=4		Ratio=8		Ratio=16	
	PSNR \uparrow	$\Delta E\downarrow$	PSNR \uparrow	$\Delta E\downarrow$	PSNR \uparrow	$\Delta E\downarrow$	PSNR \uparrow	$\Delta E\downarrow$
DeepHDR[35]	39.4902	2.0670	39.2987	2.1201	40.3268	1.9159	38.8450	2.1648
NHDRNet[39]	30.4292	5.2132	30.5489	5.0771	30.6833	5.1679	30.0553	5.3945
UNet-SID[3]	39.6099	2.1527	39.4473	2.1860	40.4429	1.9640	38.9394	2.3081
SGN[10]	39.3674	2.3317	39.3531	2.3357	40.0126	2.1956	38.7366	2.4639
AHDRNet[36]	40.4131	2.0123	40.4692	1.9829	41.0748	1.8519	39.6953	2.2025
Ours	40.5238	1.9568	40.4061	1.9743	41.4010	1.7974	39.7642	2.0988

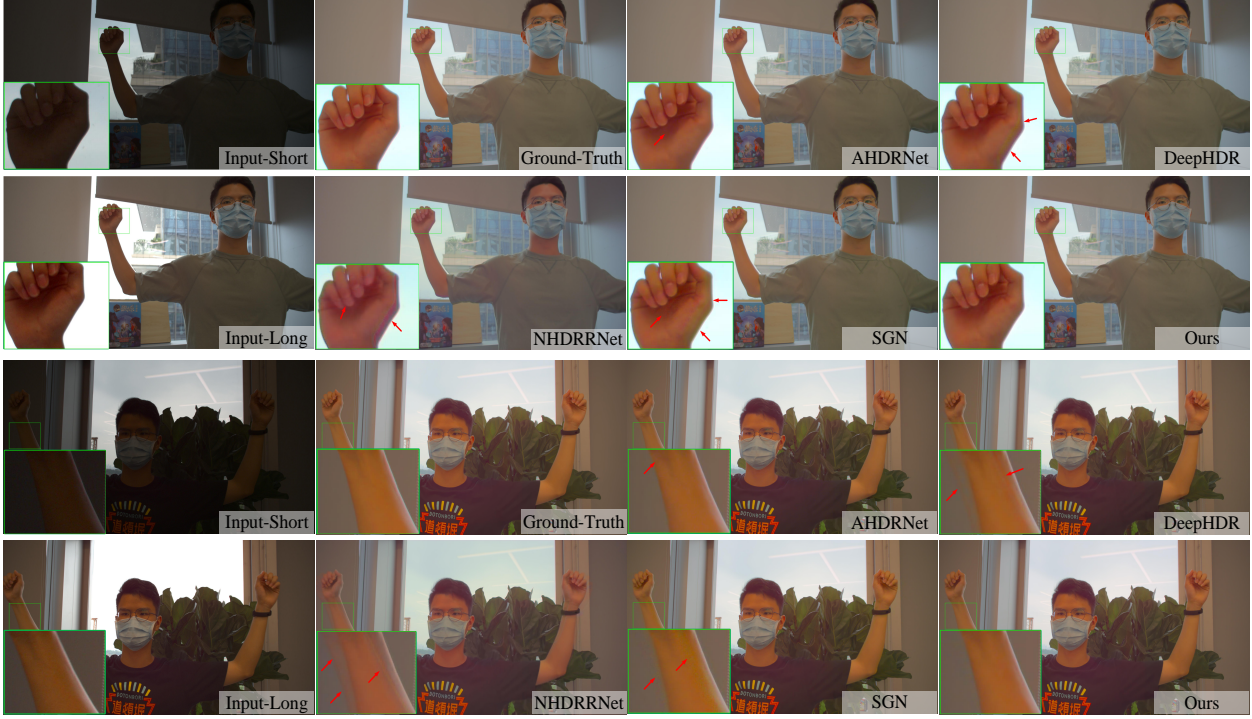


Figure 6. Visual comparisons on the testing data from Chen’s dataset [5].

Evaluation Metrics. We conduct quantitative evaluation using the peak signal-to-noise ratio (PSNR) and ΔE [43, 12]. ΔE measures the difference between two HDR images in CIE lab color space: $\Delta E = \|\tilde{I}_{lab}^{out} - I_{lab}^{gt}\|_2$, where \tilde{I}_{lab}^{out} and I_{lab}^{gt} are the CIE Lab version of the predicted HDR image and ground truth, respectively.

5.2. Implementation Details

We train our model with the Adam optimizer [17] with weight decay 1×10^4 , learning rate $1e - 4$, and $\beta_1 = 0.9$, $\beta_2 = 0.999$. The network input patch size is 256×256 and the batch size is 32. Our model is implemented in PyTorch and trained with an NVIDIA RTX 3090 GPU.

5.3. Comparison with the State-of-the-art Methods

We choose a few representative low-level vision methods for comparisons, including three HDR methods based on sRGB images (AHDRNet [36], DeepHDR [35], NHDRNet [39]) and two raw images denoising methods (SGN

[10] and UNet-SID [3]). For a fair comparison, we retrain all the methods with the RealRaw-HDR dataset. In addition, we modify the network inputs of AHDRNet, DeepHDR, and NHDRNet to input dual-exposure raw images. Similarly, for SGN and UNet-SID, we concatenate the long- and short-exposure images as input.

The quantitative comparison results are shown in Tab. 1 and Tab. 2. Compared with previous methods, our approach achieves state-of-the-art performance in terms of both visual quality and quantitative metrics. Results in Tab. 1 show that our method achieves more than 0.1 dB and 0.01 gain in terms of PSNR and ΔE , respectively, compared to AHDRNet [36] for scenes with an exposure ratio of 16. Tab. 2 shows our method achieves more than 0.1 dB and 0.05 gain on average. As shown in Fig. 5, DeepHDR [35], NHDRNet [39], and SGN [10] exhibit many artifacts in the palm motion region; NHDRNet has a large color bias as shown in Fig. 6. The proposed RepUNet can produce high-quality results with fewer artifacts and better colors.

Table 3. Quantitative comparisons of different loss functions.

ID	Method	Bayer-Loss	MA-Loss	All-Exposure		Ratio=4		Ratio=8		Ratio=16	
				PSNR \uparrow	$\Delta E \downarrow$	PSNR \uparrow	$\Delta E \downarrow$	PSNR \uparrow	$\Delta E \downarrow$	PSNR \uparrow	$\Delta E \downarrow$
1	RepUNet	\times	\times	39.6403	2.1479	39.5214	2.1577	40.5216	1.9603	38.8780	2.3256
2	RepUNet	\checkmark	\times	40.0251	2.1162	39.9900	2.1143	40.8125	1.9700	39.2729	2.2642
3	RepUNet	\checkmark	\checkmark	40.5238	1.9568	40.4061	1.9743	41.4010	1.7974	39.7642	2.0988

Table 4. Re-parameterization ablation results. The FLOPs and Run Times are measured on the raw image of 4K resolution.

Method	FLOPs	Params	Run Times	All-Exposure		Ratio=4		Ratio=8		Ratio=16	
				PSNR \uparrow	$\Delta E \downarrow$	PSNR \uparrow	$\Delta E \downarrow$	PSNR \uparrow	$\Delta E \downarrow$	PSNR \uparrow	$\Delta E \downarrow$
Base Model	93.26G	0.82M	3.0 ms	39.7941	2.1202	39.8026	2.1036	40.5092	1.9790	39.0705	2.2780
RepUNet _{worp}	250.79G	2.16M	70.1 ms	40.5220	1.9573	40.4051	1.9746	41.3990	1.7978	39.7620	2.0995
RepUNet	93.26G	0.82M	2.9 ms	40.5238	1.9568	40.4061	1.9743	41.4010	1.7974	39.7642	2.0988

In particular, our lightweight-efficient RepUNet model has fewer parameters and extremely low GFLOPs. Hence, we can process a 4K Bayer input with only 2.9ms on an NVIDIA RTX 3090 GPU, while other models with comparable performance require a significantly longer time. RepUNet achieves comparable performance with AHDRNet with only 4.5% of its computational complexity (127G vs. 2848G). Moreover, the alignment module in DeepHDR, AHDRNet, and NHDRNet will occupy a large number of line buffers, which is difficult to deploy on resource-limited edge devices. Our method can alleviate ghost artifacts without relying on the alignment module and mitigate the color cast problem of the raw image, as shown in Fig. 5 and Fig. 6 the visual results. Notably, we train the models on our RealHDR-Raw dataset and still achieve promising results on Chen’s dataset. This demonstrates the generalizability of our proposed dataset and method, indicating the robustness of our approach and its potential for real-world applications.

5.4. Ablation Study

This section investigates the raw HDR data formation pipeline and the importance of different components in the whole RepUNet. We ablate the baseline model step by step and compare the performance differences.

Generalization of Our HDR Data Formation. Our HDR data formation pipeline is proposed to generate paired raw HDR data but can be also adopted for the generation of paired sRGB HDR data. To demonstrate such generalization, we transform the collected RealRaw-HDR dataset with a fixed ISP pipeline into the sRGB color space, named RAW2RGB-HDR dataset. For comparison, we train the sRGB HDR method AHDRNet [36] on our RAW2RGB-HDR dataset (240 pairs) and Kalantari’s dataset [16] (taking the first two exposure as input, 74 pairs of images), respectively. The test dataset is from Kalantari’s dataset. Results in Tab. 5 show that AHDRNet trained on our RAW2RGB-HDR dataset outperforms the one trained on Kalantari’s dataset by 2.86 dB in PSNR. It benefits from an efficient and user-friendly pipeline for acquiring data, allowing for more trainable data pairs. The results demonstrate that our

data pipeline is also effective in generating paired LDR-HDR data in sRGB space.

Table 5. Extension of our data pipeline for sRGB HDR.

Method	Dataset	PSNR	PSNR- μ
AHDRNet	Kalantari	35.4581	38.1618
	RAW2RGB-HDR	38.3183	39.8896

Study on Loss Functions. To test the effects of motion alignment loss and Bayer loss, we set the $L2$ loss with L_{ssim} as the baseline and step-by-step modify the loss function combination. Tab. 3 shows that adding the sub-loss functions steadily improves the results. The full loss achieves the best results, outperforming the baseline by 0.5 dB in PSNR and by 0.16 in ΔE on average. As Fig. 7 shows motion alignment (MA) loss and Bayer loss can effectively suppress artifacts and color cast.

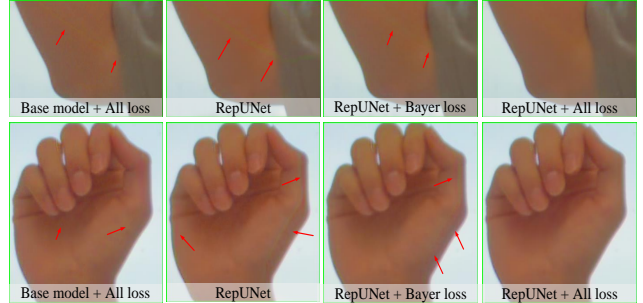


Figure 7. Visual results of RepUNet and its baseline variants.

Study on Model Re-parameterization. Tab. 4 presents the results for the base model, RepUNet without reparameterization (RepUNet_{worp}), and RepUNet with reparameterization. RepUNet enjoys the same low complexity as the base model, and shares even slightly higher reconstruction performance than RepUNet_{worp}, which validates the effectiveness of our proposed TCB module.

6. Conclusion

We designed an HDR data formation pipeline based on computational photography and constructed the first

raw HDR dataset. This dataset provides training data for raw HDR image reconstruction. Based on this dataset, we propose a lightweight-efficient RepUNet network based on structural re-parameterization for HDR reconstruction. Meanwhile, we propose a plug-and-play motion alignment loss and Bayer loss to alleviate the image alignment problem and avoid color cast. Extensive experiments demonstrate that our approach achieves state-of-the-art performance in both visual quality and quantitative metrics.

References

- [1] SM A Sharif, Rizwan Ali Naqvi, and Mithun Biswas. Beyond joint demosaicking and denoising: An image processing pipeline for a pixel-bin image sensor. In *Proceedings of the IEEE/CVF Conference on Computer Vision and Pattern Recognition*, pages 233–242, 2021.
- [2] Mark Buckler, Suren Jayasuriya, and Adrian Sampson. Reconfiguring the imaging pipeline for computer vision. In *Proceedings of the IEEE International Conference on Computer Vision*, pages 975–984, 2017.
- [3] Chen Chen, Qifeng Chen, Jia Xu, and Vladlen Koltun. Learning to see in the dark. In *Proceedings of the IEEE conference on computer vision and pattern recognition*, pages 3291–3300, 2018.
- [4] Chengpeng Chen, Zichao Guo, Haien Zeng, Pengfei Xiong, and Jian Dong. Repghost: A hardware-efficient ghost module via re-parameterization. *arXiv preprint arXiv:2211.06088*, 2022.
- [5] Guanying Chen, Chaofeng Chen, Shi Guo, Zhetong Liang, Kwan-Yee K Wong, and Lei Zhang. Hdr video reconstruction: A coarse-to-fine network and a real-world benchmark dataset. In *Proceedings of the IEEE/CVF International Conference on Computer Vision*, pages 2502–2511, 2021.
- [6] L. Chermak and N. Aouf. Enhanced feature detection and matching under extreme illumination conditions with a hdr imaging sensor. In *IEEE International Conference on Cybernetic Intelligent Systems*, 2012.
- [7] Xiaohan Ding, Yuchen Guo, Guiguang Ding, and Jungong Han. Acnet: Strengthening the kernel skeletons for powerful cnn via asymmetric convolution blocks. In *Proceedings of the IEEE/CVF international conference on computer vision*, pages 1911–1920, 2019.
- [8] Xiaohan Ding, Xiangyu Zhang, Jungong Han, and Guiguang Ding. Diverse branch block: Building a convolution as an inception-like unit. In *Proceedings of the IEEE/CVF Conference on Computer Vision and Pattern Recognition*, pages 10886–10895, 2021.
- [9] Xiaohan Ding, Xiangyu Zhang, Ningning Ma, Jungong Han, Guiguang Ding, and Jian Sun. Repvgg: Making vgg-style convnets great again. In *Proceedings of the IEEE/CVF conference on computer vision and pattern recognition*, pages 13733–13742, 2021.
- [10] Shuhang Gu, Yawei Li, Luc Van Gool, and Radu Timofte. Self-guided network for fast image denoising. In *Proceedings of the IEEE/CVF International Conference on Computer Vision*, pages 2511–2520, 2019.
- [11] Glenn E Healey and Raghava Kondepudy. Radiometric ccd camera calibration and noise estimation. *IEEE Transactions on Pattern Analysis and Machine Intelligence*, 16(3):267–276, 1994.
- [12] Bernhard Hill, Th Roger, and Friedrich Wilhelm Vorhagen. Comparative analysis of the quantization of color spaces on the basis of the cielaab color-difference formula. *ACM Transactions on Graphics (TOG)*, 16(2):109–154, 1997.
- [13] Berthold KP Horn and Robert W Sjöberg. Calculating the reflectance map. *Applied optics*, 18(11):1770–1779, 1979.
- [14] Huimin Huang, Lanfen Lin, Ruofeng Tong, Hongjie Hu, Qiaowei Zhang, Yutaro Iwamoto, Xianhua Han, Yen-Wei Chen, and Jian Wu. Unet 3+: A full-scale connected unet for medical image segmentation. In *ICASSP 2020-2020 IEEE International Conference on Acoustics, Speech and Signal Processing (ICASSP)*, pages 1055–1059. IEEE, 2020.
- [15] A. Huggett, C. Silsby, S. Cami, and J. Beck. A dual-conversion-gain video sensor with dewarping and overlay on a single chip. In *IEEE International Solid-state Circuits Conference-digest of Technical Papers*, 2009.
- [16] Nima Khademi Kalantari, Ravi Ramamoorthi, et al. Deep high dynamic range imaging of dynamic scenes. *ACM Trans. Graph.*, 36(4):144–1, 2017.
- [17] Diederik P. Kingma and Jimmy Ba. Adam: A method for stochastic optimization. *arXiv: Learning*, 2014.
- [18] S. Lee, G. H. An, and S. J. Kang. Deep chain hdri: Reconstructing a high dynamic range image from a single low dynamic range image, 2018.
- [19] Zhen Liu, Wenjie Lin, Xinpeng Li, Qing Rao, Ting Jiang, Mingyan Han, Haoqiang Fan, Jian Sun, and Shuaicheng Liu. Adnet: Attention-guided deformable convolutional network for high dynamic range imaging. In *Proceedings of the IEEE/CVF Conference on Computer Vision and Pattern Recognition*, pages 463–470, 2021.
- [20] Zhen Liu, Yinglong Wang, Bing Zeng, and Shuaicheng Liu. Ghost-free high dynamic range imaging with context-aware transformer. In *Computer Vision—ECCV 2022: 17th European Conference, Tel Aviv, Israel, October 23–27, 2022, Proceedings, Part XIX*, pages 344–360. Springer, 2022.
- [21] K. Ma, Z. Duanmu, H. Zhu, Y. Fang, and Z. Wang. Deep guided learning for fast multi-exposure image fusion, 2019.
- [22] Ymir Mäkinen, Lucio Azzari, and Alessandro Foi. Collaborative filtering of correlated noise: Exact transform-domain variance for improved shrinkage and patch matching. *IEEE Transactions on Image Processing*, 29:8339–8354, 2020.
- [23] J. S. McElvain, W. C. Gish, J. R. Miller, G. J. Ward, and R. Atkins. Auto exposure of spatially-multiplexed-exposure high-dynamic-range image sensors, 2021.
- [24] S. K. Nayar. High dynamic range imaging: spatially varying pixel exposures. In *IEEE Conference on Computer Vision & Pattern Recognition Cvpr*, 2002.
- [25] Nima Khademi, Kalantari, Ravi, and Ramamoorthi. Deep hdr video from sequences with alternating exposures. *Computer graphics forum : journal of the European Association for Computer Graphics*, 38(2):193–205, 2019.
- [26] Y. Niu, J. Wu, W. Liu, W. Guo, and Rwh Lau. Hdr-gan: Hdr image reconstruction from multi-exposed ldr images with large motions. *arXiv e-prints*, 2020.

- [27] Niki Parmar, Ashish Vaswani, Jakob Uszkoreit, Lukasz Kaiser, Noam Shazeer, Alexander Ku, and Dustin Tran. Image transformer. In *International conference on machine learning*, pages 4055–4064. PMLR, 2018.
- [28] K Ram Prabhakar, Susmit Agrawal, Durgesh Kumar Singh, Balraj Ashwath, and R Venkatesh Babu. Towards practical and efficient high-resolution hdr deghosting with cnn. In *Computer Vision–ECCV 2020: 16th European Conference, Glasgow, UK, August 23–28, 2020, Proceedings, Part XXI 16*, pages 497–513. Springer, 2020.
- [29] Guocheng Qian, Yuanhao Wang, Jinjin Gu, Chao Dong, Wolfgang Heidrich, Bernard Ghanem, and Jimmy S Ren. Rethinking learning-based demosaicing, denoising, and super-resolution pipeline. In *2022 IEEE International Conference on Computational Photography (ICCP)*, pages 1–12. IEEE, 2022.
- [30] Mushfiqur Rouf, Rafal Mantiuk, Wolfgang Heidrich, Matthew Trentacoste, and Cheryl Lau. Glare encoding of high dynamic range images. *Computer Vision and Pattern Recognition*, 2011.
- [31] Victor Sanh, Lysandre Debut, Julien Chaumond, and Thomas Wolf. Distilbert, a distilled version of bert: smaller, faster, cheaper and lighter. *arXiv preprint arXiv:1910.01108*, 2019.
- [32] Q. Sun, E. Tseng, Q. Fu, W. Heidrich, and F. Heide. Learning rank-1 diffractive optics for single-shot high dynamic range imaging. In *cvpr*, 2020.
- [33] Yuzhi Wang, Haibin Huang, Qin Xu, Jiaming Liu, Yiqun Liu, and Jue Wang. Practical deep raw image denoising on mobile devices. In *Computer Vision–ECCV 2020: 16th European Conference, Glasgow, UK, August 23–28, 2020, Proceedings, Part VI*, pages 1–16. Springer, 2020.
- [34] Kaixuan Wei, Ying Fu, Jiaolong Yang, and Hua Huang. A physics-based noise formation model for extreme low-light raw denoising. In *Proceedings of the IEEE/CVF Conference on Computer Vision and Pattern Recognition*, pages 2758–2767, 2020.
- [35] Shangzhe Wu, Jiarui Xu, Yu-Wing Tai, and Chi-Keung Tang. Deep high dynamic range imaging with large foreground motions. In *Proceedings of the European Conference on Computer Vision (ECCV)*, pages 117–132, 2018.
- [36] Q. Yan, D. Gong, Q. Shi, Avd Hengel, and Y. Zhang. Attention-guided network for ghost-free high dynamic range imaging. In *2019 IEEE/CVF Conference on Computer Vision and Pattern Recognition (CVPR)*, 2019.
- [37] Q. Yan, D. Gong, P. Zhang, Q. Shi, J. Sun, I. Reid, and Y. Zhang. Multi-scale dense networks for deep high dynamic range imaging. In *Workshop on Applications of Computer Vision*, 2019.
- [38] Q. Yan, L. Zhang, Y. Liu, Y. Zhu, J. Sun, Q. Shi, and Y. Zhang. Deep hdr imaging via a non-local network. *IEEE Transactions on Image Processing*, 29:4308–4322, 2020.
- [39] Qingsen Yan, Lei Zhang, Yu Liu, Yu Zhu, Jinqiu Sun, Qinfeng Shi, and Yanning Zhang. Deep hdr imaging via a non-local network. *IEEE Transactions on Image Processing*, 29:4308–4322, 2020.
- [40] Z. Yan and J. Fang. The low-frequency noise of hgcdte sensor with overlap structure. In *Noise and Information in Nanoelectronics, Sensors, and Standards II*, 2004.
- [41] Huanjing Yue, Cong Cao, Lei Liao, Ronghe Chu, and Jingyu Yang. Supervised raw video denoising with a benchmark dataset on dynamic scenes. In *Proceedings of the IEEE/CVF conference on computer vision and pattern recognition*, pages 2301–2310, 2020.
- [42] Xuaner Zhang, Qifeng Chen, Ren Ng, and Vladlen Koltun. Zoom to learn, learn to zoom. In *Proceedings of the IEEE/CVF Conference on Computer Vision and Pattern Recognition*, pages 3762–3770, 2019.
- [43] Xuemei Zhang, Brian A Wandell, et al. A spatial extension of cielab for digital color image reproduction. In *SID international symposium digest of technical papers*, volume 27, pages 731–734. Citeseer, 1996.
- [44] Xindong Zhang, Hui Zeng, and Lei Zhang. Edge-oriented convolution block for real-time super resolution on mobile devices. In *Proceedings of the 29th ACM International Conference on Multimedia*, pages 4034–4043, 2021.
- [45] Yi Zhang, Hongwei Qin, Xiaogang Wang, and Hongsheng Li. Rethinking noise synthesis and modeling in raw denoising. In *Proceedings of the IEEE/CVF International Conference on Computer Vision*, pages 4593–4601, 2021.